RSC Advances

PAPER

View Article Online
View Journal | View Issue

Cite this: *RSC Adv.*, 2022, **12**, 1527

Improving the properties of Fe_2O_3 by a sparking method under a uniform magnetic field for a high-performance humidity sensor

Posak Tippo,[ab] Pisith Singjai,[a] Waraporn Sroila,[a] Tipsuda Jaisamer,[a] Nongpanita Suttanon,[a] Arisara Panthawan,[a] Ekkapong Kantarak,[a] Wattikon Sroila,[a] Wiradej Thongsuwan,[a] Tewasin Kumpika[ab] and Orawan Wiranwetchayan*[bc]

Iron oxide (Fe_2O_3) thin films are promising semiconductors for electronic applications because Fe_2O_3 is an earth-abundant semiconductor with an appropriate band gap. However, many methods for the synthesis of Fe_2O_3 thin films require a corrosive source, complex procedures, and many types of equipment. Here, we report, for the first time, a simple method for Fe_2O_3 deposition using sparking under a uniform magnetic field. The morphology of Fe_2O_3 displayed an agglomeration of particles with a network-like structure. The crystallite size, % Fe content, and optical bandgap of Fe_2O_3 were influenced by changes in the magnitude of the magnetic field. For application in humidity sensors, Fe_2O_3 at a magnetic field of 200 mT demonstrated a sensitivity of 99.81%, response time of 0.33 s, and recovery time of 2.57 s. These results can provide references for new research studies.

Received 9th October 2021
Accepted 15th December 2021

DOI: 10.1039/d1ra07490c

rsc.li/rsc-advances

Introduction

Iron oxide (Fe_2O_3) plays an important part in many applications (*e.g.*, gas sensors, batteries, supercapacitors, and photocatalytic water splitting) because Fe_2O_3 is an earth-abundant semiconductor with a direct bandgap of ~2.35 eV and an indirect bandgap of ~1.38 eV.[1–6] Moreover, Fe_2O_3 nanoparticles coated with fullerene-like shells are also used as "nano-transporters" for radioisotopes, which is beneficial for diagnosing and monitoring in the medical field.[2] A high surface area and surface-to-volume ratio with surface modification enables Fe_2O_3 nanoparticle films to become appropriate materials for humidity sensors.[7] Nevertheless, many methods for the synthesis of Fe_2O_3 thin films (*e.g.*, sputtering and atomic layer deposition) require different types of equipment and involve complex procedures.[8,9] In addition, the fabrication of humidity sensor-based Fe_2O_3 requires a temperature > 1000 °C, for example, for the sintering method.[10,11] Therefore, an alternative method with a simple process and low temperature requirement for the synthesis of Fe_2O_3 thin films is essential.

It has been reported that facile methods such as sparking under a non-uniform magnetic field can influence the properties of magnetic materials such as iron (Fe), nickel (Ni) and cobalt (Co).[12,13] Previously, we showed that an increase in the magnitude of a uniform magnetic field reduces the porosity and improves the crystal structure as well as the electrical properties of a NiO film.[14,15] Thus, a sparking method under a uniform magnetic field could be employed to produce a Fe_2O_3 film and optimize its properties for humidity sensors.

Here, we reveal, for the first time, Fe_2O_3 deposition using a sparking method under a uniform magnetic field. The influence of the magnetic field on the morphology, crystal structure, optical properties, chemical composition, and electrical properties was studied. Furthermore, the capability of the Fe_2O_3 film to sense humidity was investigated.

Experimental section

Deposition of Fe_2O_3

A glass substrate of area 1 × 1 cm^2 was cleaned by sonication for 5 min each time in deionized (DI) water, acetone, and ethanol, respectively. The sparking method under a uniform magnetic field of 0, 100, 200, and 300 mT was setup according to our previous work (Fig. 1).[15] Fe wires (99.98% purity; Advent Research Materials) were deposited onto the glass substrate for 30 min. Then, films were annealed at 450 °C under ambient air for 2 h.

Fabrication of humidity sensor

Interdigitated electrodes (IDEs) with an area of 1 × 1.5 cm^2 and a channel of 450 μm were cleaned by sonication and deposited by the sparking method under a uniform magnetic field, as

[a]*Department of Physics and Materials Science, Faculty of Science, Chiang Mai University, Chiang Mai 50200, Thailand*

[b]*Center of Excellence in Materials Science and Technology, Chiang Mai University, Chiang Mai 50200, Thailand*

[c]*Research Center in Physics and Astronomy, Faculty of Science, Chiang Mai University, Chiang Mai 50200, Thailand. E-mail: wiranwetchayan@gmail.com*

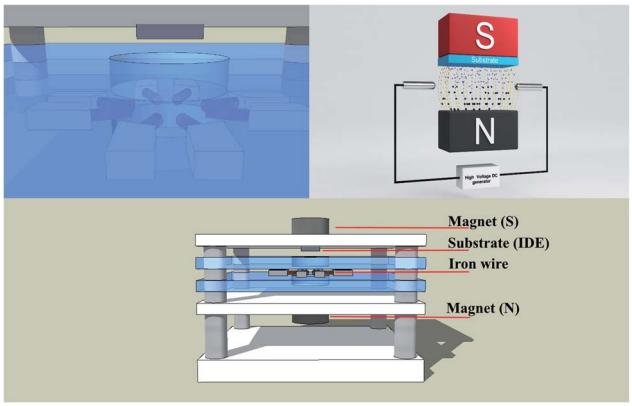

Fig. 1 Deposition of Fe_2O_3 and fabrication of a humidity sensor (schematic).[15]

mentioned above. The deposition time for each condition was 5 h.

Characterization

Fe_2O_3 films were characterized by scanning electron microscopy (SEM) using a JSM-6335F system (Jeol), X-ray diffraction spectrometry (XRD) employing an X0Pert MPD setup (Philips), ellipsometry using an alpha-SE system (JA Woollam), UV-Vis spectrophotometry employing a Varian Cary 50 setup (Agilent Technologies) and X-ray photoelectron spectrometry (XPS) using an Axis Ultra DLD system (Kratos Analytical). Fe_2O_3 humidity sensors were evaluated using a source measure unit (2450 series; Keithley Instruments) and a humidity controller (Fig. 2).

Results and discussion

SEM (Fig. 3) displayed the morphology of Fe_2O_3 deposited at various magnitudes of the magnetic field. SEM images revealed the agglomeration of particles with a network-like structure. Moreover, the increase in the magnitude of the magnetic field induced accumulation of more particles. Interestingly, this result was not in accordance with our previous work, which indicated that an increase in the magnetic field reduced the porosity of the NiO film.[14,15] The reason for this result was the earlier oxidation of Fe particles without annealing, which resulted in misalignment of the particles.[12]

The crystal structure of Fe_2O_3 films analyzed by XRD is displayed in Fig. 4a. The patterns of the Fe_2O_3 films at a magnetic field of 0 mT did not contain any peaks. For Fe_2O_3 films at magnetic fields of 100–300 mT, all peaks were in accordance with Joint Committee on Powder Diffraction Standards (JCPDS) 33-0664, which revealed the film deposited by our method to be hematite (α-Fe_2O_3). Increasing the magnetic field up to 200 mT increased the intensity of the (104) peak and decreased after the magnetic field exceeded 200 mT. To obtain the crystallite size (D) and dislocation density (δ) of Fe_2O_3 films, we used the following equation:[15]

$$D = 0.9\lambda/\beta \cos\theta \quad (1)$$

$$\delta = \frac{1}{D^2} \quad (2)$$

where λ is the wavelength of the X-ray (1.5418 Å), β is the full width at half maximum (FWHM) of the diffraction peak and θ is the Bragg angle of the diffraction peak. This equation revealed that the crystallite size of Fe_2O_3 films at a magnetic field of 100, 200, and 300 mT was 39.2, 41.5 and 30.2 nm, respectively. For a dislocation density of Fe_2O_3 films at a magnetic field of 100, 200, and 300 mT, the value calculated by eqn (2) was 6.52, 5.81 and 1.1 $\times$ 10^{15} lines m^{-2}, respectively.

The optical properties of Fe_2O_3 films are shown in Fig. 4b and c. The absorption spectra in Fig. 4b reveal that the increase in the magnitude of the magnetic field from 0 mT to 200 mT causes a redshift and increased the absorption intensity. However, a too-high magnetic field (300 mT) led to a blueshift, which originated from an increase in dislocation density as observed by XRD. This result is consistent with data for other metal oxides reported by Zeid and colleagues and Schwinger and collaborators.[16,17] Ellipsometry revealed the thickness of the Fe_2O_3 films at a magnetic field of 0, 100, 200, and 300 mT to be 258, 447, 641, and 901 nm, respectively. The transmittance of the Fe_2O_3 films is shown in Fig. 4c. The average transmittance (T_{avg}) of Fe_2O_3 films at a magnetic field of 0, 100, 200, and 300 mT was 85.65%, 80.70%, 68.04%, and 59.46%, respectively. This result is in accordance with the increase in film thickness measured by ellipsometry because a stronger magnetic field can

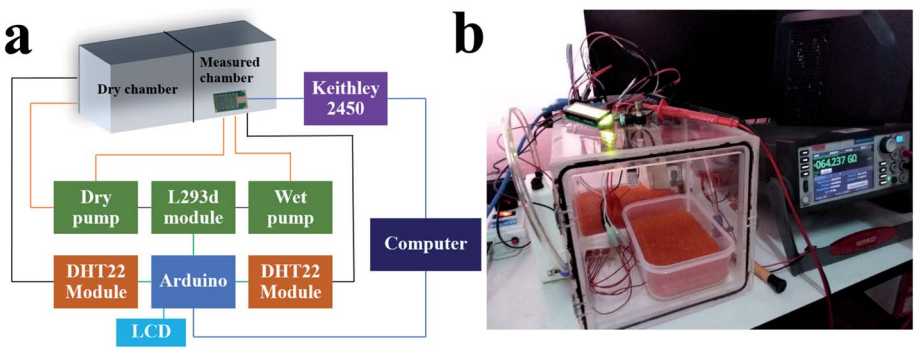

Fig. 2 (a) Schematic diagram and (b) practical use of the humidity controller.

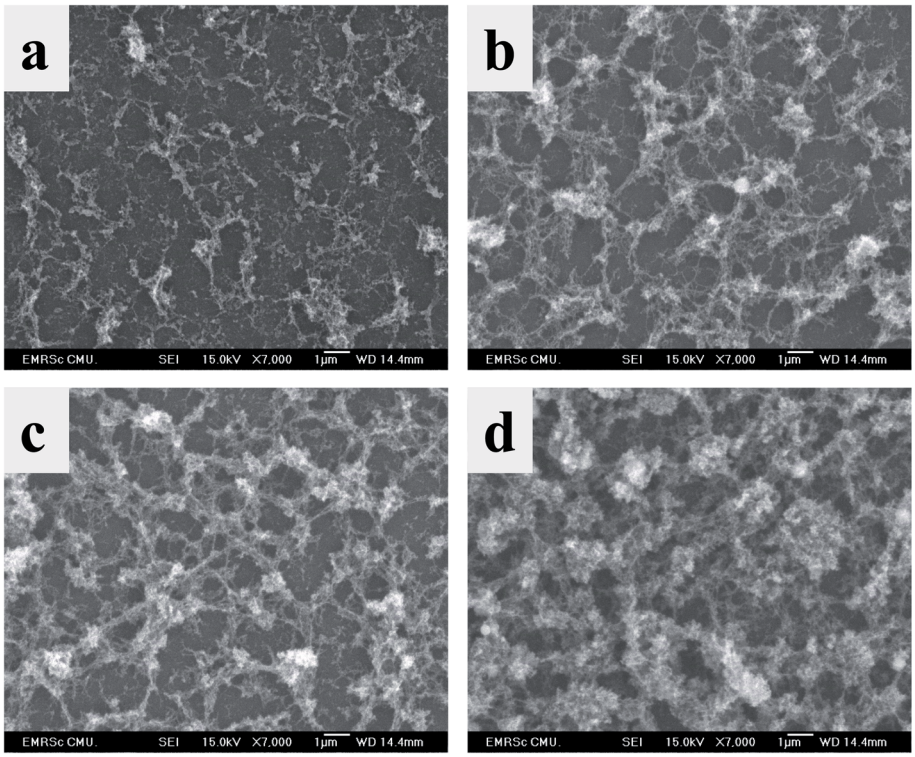

Fig. 3 SEM images of (a) 0 mT, (b) 100 mT, (c) 200 mT, and (d) 300 mT Fe_2O_3, respectively, on a glass substrate.

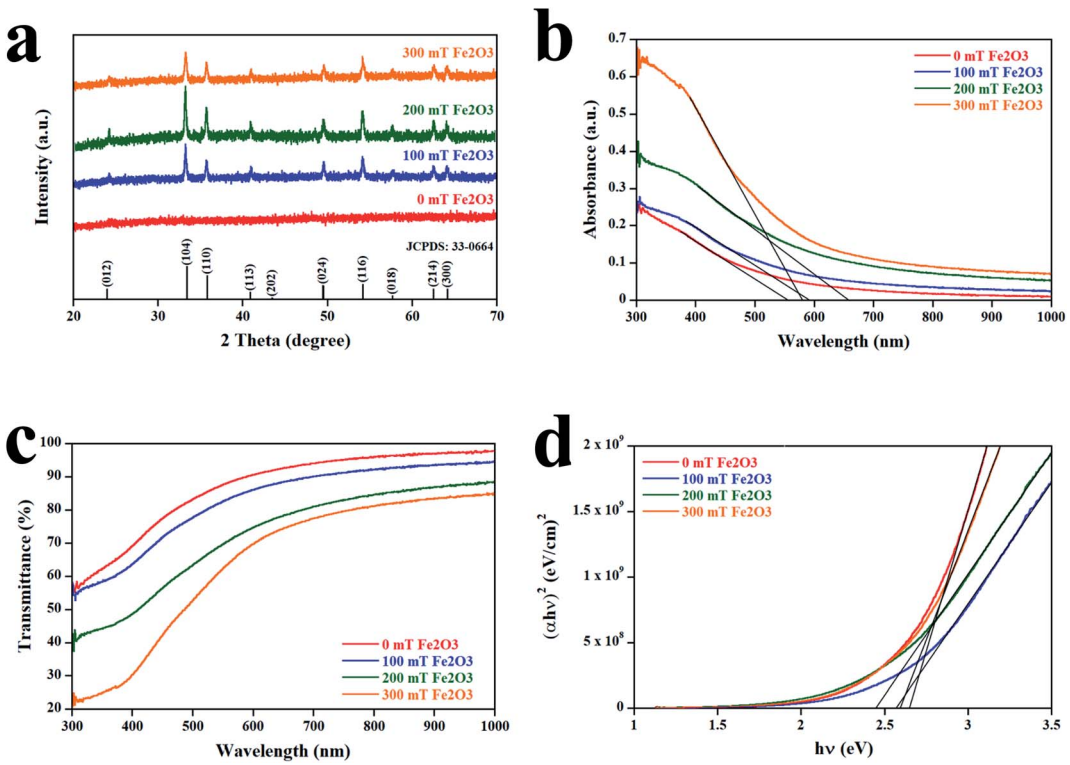

Fig. 4 (a) XRD patterns of samples. (b) Absorbance of Fe_2O_3 films. (c) Transmittance of Fe_2O_3 films. (d) Tauc plot of samples.

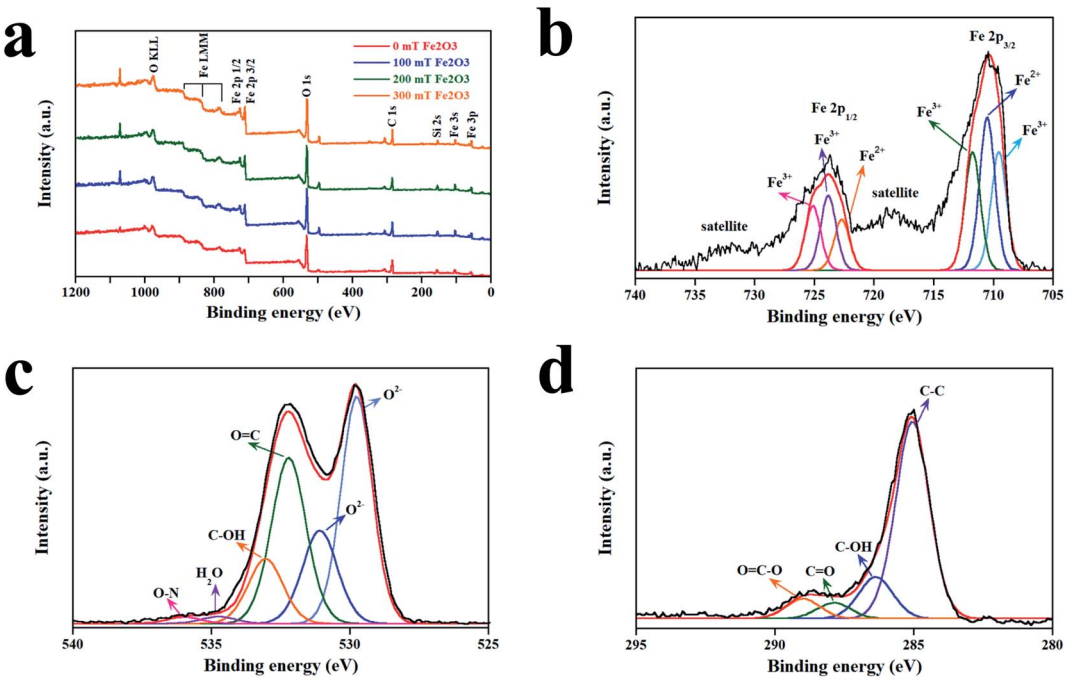

Fig. 5 XPS of Fe_2O_3 films deposited at a magnetic field of different strengths. (a) Survey scan of samples. (b) Fe 2p core-level spectrum. (c) O 1s core-level spectrum. (d) C 1s core-level spectrum.

Table 1 XPS data of samples

Peak	Position (eV)	Assignment	Reference
Fe $2p_{3/2}$	710.2	Fe^{3+}	18
	711.6	Fe^{2+}	19
	713.2	Fe^{3+}	19
Fe $2p_{1/2}$	723.6	Fe^{2+}	20
	725	Fe^{3+}	20
	726.5	Fe^{3+}	21
O 1s	530	O^{2-}	15
	531	O^{2-}	14
	532.8	O═C	22
	534	C–OH	22
	535.3	H_2O	23
	536	O–N	24
C 1s	285	C–C	25
	286.2	C–OH	15
	287	C═O	14
	289	O═C–O	15

collect more particles. To reveal the influence of the magnetic field on the bandgap (E_g) of Fe_2O_3, we used Tauc's relationship, as determined by the following equation:[14,15]

$$(\alpha h\nu) = A(h\nu - E_g)^n \quad (3)$$

$$\alpha = 2.303\left(\frac{A_b}{t}\right) \quad (4)$$

where ν is the photon frequency, h is the Planck constant, A is a proportionality constant, α is the absorption coefficient, A_b is the absorbance, t is the thickness of the film, and n is equal to 2 or 1/2 for indirect and direct transitions, respectively. By using $(\alpha h\nu)^2$ *versus* $h\nu$ (Fig. 4d), the optical bandgap of Fe_2O_3 films at a magnetic field of 0, 100, 200, and 300 mT was evaluated to be 2.65, 2.58, 2.45, and 2.60 eV, respectively. This bandgap value was in agreement with the absorbance result.

The elemental composition of the films was explored by XPS (Fig. 5). The survey spectra in Fig. 5a show that all films consisted of Fe, O, Mg, Na, Ca, C, and Si at the same location for each condition. Mg, Na, Ca, and Si originated from the glass substrate. In addition, the signal for C arose from contamination of the carbon tape, which is used as the electrical contact between the sample and the holder of XPS. By applying a magnetic field of 0, 100, 200, and 300 mT, the atomic concentration of Fe was found to be 9.47%, 10.82%, 13.06%, and 15.75%, respectively. Therefore, the increase in % Fe was in agreement with the number of particles observed by SEM. The XPS core-level spectra of Fe 2p, O 1s, and C 1s are illustrated in Fig. 5b–d, and assignment of elemental bonding is shown in Table 1.

Fig. 6 illustrates the electrical properties of the Fe_2O_3 sensor deposited at magnetic fields of different strengths. Electrical properties were characterized under 100% humidity. The current (I)–voltage (V) characteristic curves of the Fe_2O_3 sensor (Fig. 6a) were linear, revealing ohmic behavior. For the 100 mT Fe_2O_3 sensor, the device acted as an insulator and did not respond to humidity. By increasing the magnetic field, the slope of the I–V characteristic curve increased, resulting in a reduction in the resistance. However, a magnetic field >200 mT increased the resistance. This effect originates from the crystallite size, which is inversely related to the resistance.[25] Therefore, the I–V characteristic curve of the Fe_2O_3 sensor supported the XRD results. To investigate further the electrical

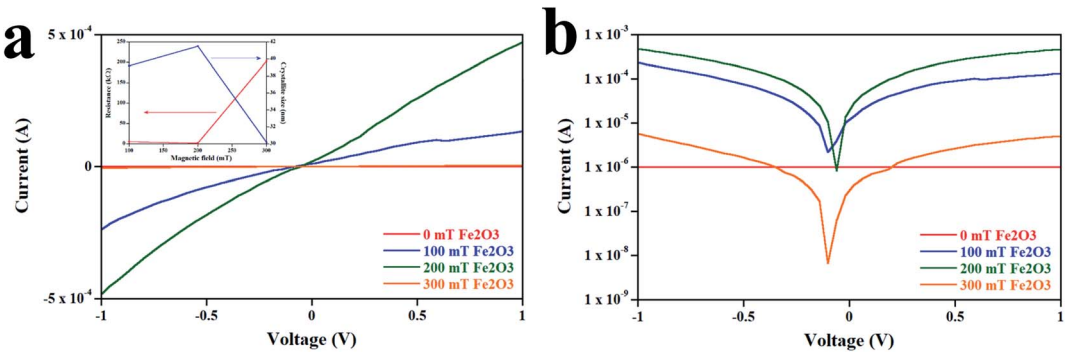

Fig. 6 Electrical properties of the Fe_2O_3 sensor at 100% humidity. (a) *I–V* characteristic curve at various magnetic fields with the inset of the resistance *versus* magnetic field (red) and crystallite size *versus* magnetic field (blue). (b) Semi-log plots of the *I–V* characteristic curve.

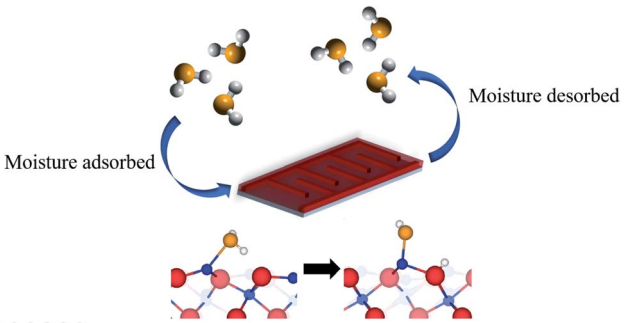

Fig. 7 Mechanism of the Fe_2O_3 humidity sensor. The blue, red, orange, and white spheres represent iron, oxygen of iron, oxygen of water, and hydrogen, respectively.[29]

properties and underlying mechanism behind the Fe_2O_3 sensor, semi-log plots of *I–V* characteristics were used (Fig. 6b). The curves of 100, 200, and 300 mT Fe_2O_3 sensors displayed negative shifts. This shift was caused by the electrochemical driving force acting on the ion, which can be explained by the following equation.[26,27]

$$I = GV_{DF} \quad (5)$$

$$V_{DF} = V_{SP} - V_O \quad (6)$$

$$R = \frac{V}{I} \quad (7)$$

where I is the ionic current, G is the conductance of the ion, V_{DF} is the electrochemical driving force, V_{SP} is the sensor potential,

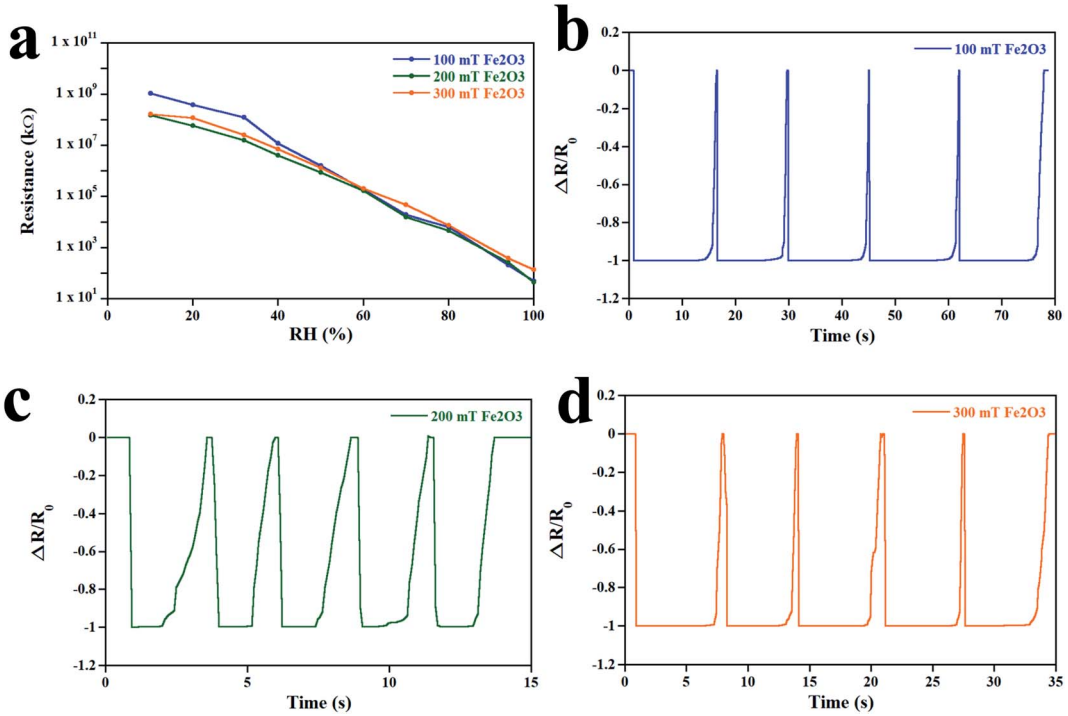

Fig. 8 (a) Resistance *versus* RH of the Fe_2O_3 sensor. The response time and recovery time of the Fe_2O_3 sensor deposited at (b) 100 mT, (c) 200 mT, and (d) 300 mT at an operating temperature of 95 °C.

Table 2 Comparative performance of humidity sensors deposited by different methods

Method	Operating temp (°C)	Response time (s)	Recovery time (s)	Reference
Spark under 100 mT	95	3.07	12.53	This work
Spark under 200 mT	95	0.33	2.57	This work
Spark under 300 mT	95	0.75	6.64	This work
Spin coating	26	1.79	4.97	28
Electrospinning	240	10.2	23	30
Hydrothermal	25	29	630	7
Hydrothermal	260	12	40	31
Carbon sphere template	380	14.5	10	32
Sputtering	—	15	40	33
Sputtering	—	3	12	34

V_O is the equilibrium potential for the oxygen ions, and R is the resistance. By considering eqn (5) and (6) at 0 V of the semi-log plots (without bias), the current has positive values ($V_{DF} > 0$), which is caused by net ionic movement across the electrode of the sensor ($V_{SP} > V_O$). This net ionic movement is generated by oxygen ions, whereas the Fe_2O_3 sensor adsorbs moisture.[28] Based on this mechanism along with eqn (7), the increase in relative humidity (RH) increases the ionic current, which results in a decrease in the resistance of the Fe_2O_3 sensor. Fig. 7 was used[29] for deeper understanding of the mechanism of the Fe_2O_3 humidity sensor.

The resistance *versus* RH of the Fe_2O_3 sensor is illustrated in Fig. 8a. Upon increasing the RH from 10% to 100%, the resistance of the Fe_2O_3 sensor decreased due to formation of a layer of water molecules, thereby generating the ionic current, as mentioned above. In addition, the lowest resistance of 100, 200, and 300 mT Fe_2O_3 sensors at an RH of 100% also matched the result of *I–V* curves. The response time and recovery time of the Fe_2O_3 sensor are shown in Fig. 8b–d. These measurements were made at a humidity of 0% to 100% at 95 °C. The average response time of 100, 200, and 300 mT Fe_2O_3 sensors was 3.07, 0.33, and 0.75 s, respectively. The average recovery time of the 100, 200, and 300 mT Fe_2O_3 sensors was 12.53, 2.57, and 6.64 s, respectively. The decrease in the response time is related to the increase in the surface area and surface-to-volume ratio.[7] An increment in these two factors also enhances heat transfer from the sensor to moisture, and decreases the recovery time, as observed in 100 and 200 mT Fe_2O_3 sensors. The response time and recovery time of the 300 mT Fe_2O_3 sensor increased due to its thickness, which caused an increase in the penetration time and time needed to release moisture. For more information on the sensitivity (S) of the sensors, eqn (8) was used:[28]

$$S = \frac{\Delta R}{R_0} \times 100 \quad (8)$$

where ΔR is the change in resistance and R_0 is the resistance at an RH of 0%. Using eqn (8), the sensitivity of 100, 200, and 300 mT Fe_2O_3 sensors was calculated to be 99.58%, 99.81%, and 99.71%, respectively. The comparative performance of humidity sensors is shown in Table 2.

The stability of 100, 200, and 300 mT sensors was measured under a humidity of 100% for 1000 min at room temperature (Fig. 9a). The 100, 200, and 300 mT sensors showed stable behavior with an average resistance (in Ω) of 11 427 ± 5, 6535 ± 2, and 403 322 ± 219, respectively. The resistance of 21 sensors deposited by sparking under a magnetic field of 200 mT is displayed in Fig. 9b. All devices were measured at a humidity of 100%.

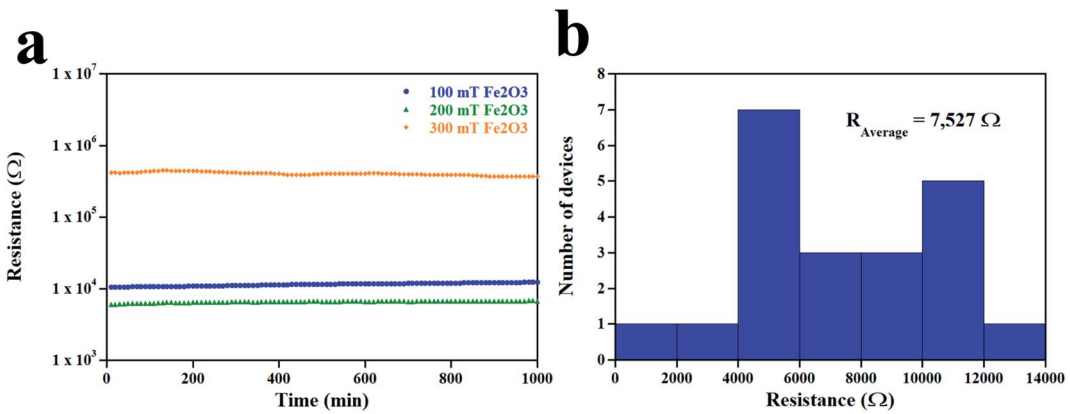

Fig. 9 (a) Stability of sensors under a humidity of 100% for 1000 min at room temperature. (b) Resistance of 21 devices deposited at a magnetic field of 200 mT.

Conclusions

Fe_2O_3 film was deposited on IDEs and a glass substrate by sparking under a uniform magnetic field. The XRD pattern and SEM revealed that the structure of the Fe_2O_3 film was hematite and network-like. The crystallite size, optical bandgap, thickness, and electrical properties of Fe_2O_3 films were influenced by the uniform magnetic field. The performance of humidity sensors based on Fe_2O_3 film can be improved by deposition at a magnetic field of 200 mT to provide a sensitivity of 99.81%, response time of 0.33 s, and recovery time of 2.57 s, at 95 °C. Our results pave the way for future investigation of the properties and applications of magnetic materials, which can be deposited by sparking under a uniform magnetic field.

Funding

This work was funded by the Research Center in Physics and Astronomy, Chiang Mai University, and the National Research and Innovation Information System, Thailand (FF65/074).

Author contributions

P. T., P. S., and O. W. designed the study, deposited the Fe_2O_3 films, and measured the sensors. E. K. and W. S. undertook XRD, UV-Vis spectroscopy, and XPS. W. T. and T. K. provided conceptual advice. W. S., T. J., N. S., and A. P. undertook SEM and created *I–V* curves.

Conflicts of interest

There are no conflicts to declare.

Acknowledgements

The authors thank the Department of Physics and Materials Science, Chiang Mai University, for use of their facilities. This research project was supported by Fundamental Found 2022, Chiang Mai University.

Notes and references

1 A. J. Deotale and R. V. Nandedkar, *Mater. Today: Proc.*, 2016, **3**, 2069.
2 L. Machala, *J. Phys. Chem. B*, 2007, **111**, 4003.
3 G. Jain, C. J. Capozzi and J. J. Xu, *J. Electrochem. Soc.*, 2003, **150**, A806.
4 D. Mao, J. Yao, X. Lai, M. Yang, J. Du and D. Wang, *Small*, 2011, **7**, 578.
5 R. Yu, Z. Li, D. Wang, X. Lai, C. Xing, M. Yang and X. Xing, *Scr. Mater.*, 2010, **63**, 155.
6 Y. Gao, R. Zhou, D. Wang, Q. Huang, C.-H. Cheng and Z. Zheng, *Chem. Res. Chin. Univ.*, 2020, **36**, 97.
7 U. V. Patil, C. S. Rout and D. J. Late, *Adv. Device Mater.*, 2015, **1**, 88.
8 M. Aronniemi, J. Saino and J. Lahtinen, *Thin Solid Films*, 2008, **516**, 6110.
9 K. Siroky, J. Jiresova and L. Hudec, *Thin Solid Films*, 1994, **245**, 211.
10 I. C. Cosentino, E. N. S. Muccillo and R. Muccillo, *Mater. Chem. Phys.*, 2007, **103**, 407.
11 C. Cantalini and M. Pelino, *J. Am. Ceram. Soc.*, 1992, **75**, 546.
12 S. S. Ručman, W. Punyodom, J. Jakmunee and P. Singjai, *Crystals*, 2018, **8**, 362.
13 S. S. Ručman, C. Boonruang and P. Singjai, *Crystals*, 2020, **10**, 1141.
14 P. Tippo, W. Thongsuwan, O. Wiranwetchayan, T. Kumpika, A. Tuantranont and P. Singjai, *Mater. Res. Express*, 2020, **7**, 056403.
15 P. Tippo, W. Thongsuwan, O. Wiranwetchayan, T. Kumpika, E. Kantarak and P. Singjai, *Sci. Rep.*, 2020, **10**, 15690.
16 S. P. Schwaminger, R. Surya, S. Filser, A. Wimmer, F. Weigl, P. Fraga-García and S. Berensmeier, *Sci. Rep.*, 2017, **7**, 12609.
17 E. F. A. Zeid, I. A. Ibrahem, A. M. Ali and W. A. A. Mohamed, *Results Phys.*, 2019, **12**, 562.
18 S. J. Gerber and E. Erasmus, *Mater. Chem. Phys.*, 2018, **203**, 73.
19 P. M. Hallam, M. Gomez-Mingot, D. K. Kampouris and C. E. Banks, *RSC Adv.*, 2012, **2**, 6672.
20 S. K. Shaw, S. K. Alla, S. S. Meena, R. K. Mandal and N. K. Prasad, *J. Magn. Magn. Mater.*, 2017, **434**, 181.
21 N. Luo, Y. Lin, J. Guo, E. Quattrocchi, H. Deng, J. Dong, F. Ciucci, F. Boi, C. Hu and S. Grasso, *Materials*, 2021, **14**, 2826.
22 P. Tippo, P. Singjai, S. Choopun and S. Sakulsermsuk, *Mater. Lett.*, 2018, **211**, 51.
23 C. W. Kao, P. T. Wu, M. Y. Liao, I. J. Chung, K. C. Yang, W. Y. I. Tseng and J. Yu, *Pharmaceutics*, 2018, **10**, 62.
24 C. Wechwithayakhlung, D. M. Packwood, J. Chaopaknam, P. Worakajit, S. Ittisanronnachai, N. Chanlek, V. Promarak, K. Kongpatpanich, D. J. Harding and P. Pattanasattayavong, *J. Mater. Chem. C*, 2019, **7**, 3452.
25 R. B. Vasiliev, M. N. Rumyantseva, S. G. Dorofeev, Y. M. Potashnikova, L. I. Ryabova and A. M. Gaskov, *Mendeleev Commun.*, 2004, **14**, 167.
26 A. L. Hodgkin and A. F. Huxley, *J. Physiol.*, 1952, **117**, 500.
27 D. K. Ferry, *Science*, 2012, **335**, 45.
28 M. U. Khan, G. Hassan, M. Awais and J. Bae, *Sens. Actuators, A*, 2020, **311**, 112072.
29 R. Ovcharenko, E. Voloshina and J. Sauer, *Phys. Chem. Chem. Phys.*, 2016, **18**, 25560.
30 S. Yan and Q. Wu, *J. Mater. Chem. A.*, 2015, **3**, 5982.
31 P. Sun, W. N. Wang, Y. P. Liu, Y. F. Sun, J. Ma and G. Y. Lu, *Sens. Actuators, B*, 2012, **173**, 52.
32 Y. F. Kang, L. W. Wang, Y. S. Wang, H. X. Zhang, Y. Wang, D. T. Hong, Y. Qv and S. R. Wang, *Sens. Actuators, B*, 2013, **177**, 570.
33 Q. Liang, H. Xu, J. Zhao and S. Gao, *Sens. Actuators, B*, 2012, **165**, 76–81.
34 P. K. Kannan, R. Saraswathi and J. B. B. Rayappan, *Sens. Actuator A Phys.*, 2010, **164**, 8–14.